ELSEVIER

Journal of Biomechanics 40 (2007) 3397–3403

JOURNAL OF BIOMECHANICS

www.elsevier.com/locate/jbiomech
www.JBiomech.com

Detection of trabecular bone microdamage by micro-computed tomography

Xiang Wang, Daniel B. Masse, Huijie Leng, Kevin P. Hess, Ryan D. Ross, Ryan K. Roeder, Glen L. Niebur*

Tissue Mechanics Laboratory, Department of Aerospace and Mechanical Engineering, University of Notre Dame, Notre Dame, IN 46556, USA

Accepted 10 May 2007

Abstract

Microdamage is an important component of bone quality and affects bone remodeling. Improved techniques to assess microdamage without the need for histological sectioning would provide insight into the role of microdamage in trabecular bone strength by allowing the spatial distribution of damage within the trabecular microstructure to be measured. Nineteen cylindrical trabecular bone specimens were prepared and assigned to two groups. The specimens in group I were damaged to 3% compressive strain and labeled with $BaSO_4$. Group II was not loaded, but was labeled with $BaSO_4$. Micro-computed tomography (Micro-CT) images of the specimens were obtained at 10 μm resolution. The median intensity of the treated bone tissue was compared between groups. Thresholding was also used to measure the damaged area fraction in the micro-CT scans. The histologically measured damaged area fraction, the median CT intensity, and the micro-CT measured damaged area fraction were all higher in the loaded group than in the unloaded group, indicating that the micro-CT images could differentiate the damaged specimen group from the unloaded specimens. The histologically measured damaged area fraction was positively correlated with the micro-CT measured damaged area fraction and with the median CT intensity of the bone, indicating that the micro-CT images can detect microdamage in trabecular bone with sufficient accuracy to differentiate damage levels between samples. This technique provides a means to non-invasively assess the three-dimensional distribution of microdamage within trabecular bone test specimens and could be used to gain insight into the role of trabecular architecture in microdamage formation.

Keywords: Microdamage; Cancellous bone; Computed tomography; Contrast agents; Bone mechanics

1. Introduction

Microdamage is one factor commonly associated with bone quality. The presence of microdamage decreases the apparent level mechanical properties of trabecular bone (Wachtel and Keaveny, 1997) and can propagate under loading (Wang and Niebur, 2006; Wang et al., 2005), which may increase fracture risk. Microdamage also stimulates adaptive remodeling (Burr, et al., 1985). As such, experimental studies of microdamage formation (Arthur Moore and Gibson, 2002) and propagation (Wang and Niebur, 2006; Wang et al., 2005) should improve our understanding of both bone fragility and mechanobiology. Techniques to assess microdamage that allow further mechanical testing could enhance capabilities to study microdamage effects on bone fragility. Spatial quantification of microdamage in three dimensions would also provide a means to quantify the localization of microdamage with respect to trabecular architecture and loading conditions, which could in turn provide further insight into the relative roles of microdamage and architecture in trabecular bone strength and adaptation.

Measurements of microdamage in bone, first reported by Frost in 1960 (Frost, 1960), have a long history. Bulk labeling followed by microscopic imaging of thin sections is the gold standard for quantifying damage (Burr and Stafford, 1990). However, it provides only a two-dimensional representation of the distribution and density of damage. Three-dimensional images of single microcracks in trabecular (Fazzalari et al., 1998) and cortical bone (O'Brien et al., 2000), obtained by reconstructing serial

*Corresponding author. Tel.: +1 574 631 3327; fax: +1 574 631 2144.
E-mail address: gniebur@nd.edu (G.L. Niebur).

0021-9290/$ - see front matter © 2007 Elsevier Ltd. All rights reserved.
doi:10.1016/j.jbiomech.2007.05.009

sections of two-dimensional confocal microscopy images, demonstrated that cracks were elliptical in shape (O'Brien et al., 2000). This technique is powerful for evaluating individual cracks or damaged regions, but can provide only limited information on the spatial distribution of microdamage, because the observation depth is limited to about 160 μm from the surface (Fazzalari et al., 1998; O'Brien et al., 2000) and the field of view is small. Microdamage due to non-uniform loading modes, such as torsion, has been studied by accounting for changes in the strain level (Wang and Niebur, 2006; Wang et al., 2005), but was again limited to a few two-dimensional sections for each test specimen. The use of thin sections also resulted in loss of information regarding the surrounding trabecular structure, limiting the ability to assess the effects of architecture on microdamage formation. Recently, an iodine-based, calcium-chelating contrast agent was used to image a scratch on the surface of a bone sample using micro-computed tomography (micro-CT) (Lee et al., 2003; Parkesh et al., 2006). Synchrotron radiation sources can provide very high-resolution images that allow direct visualization of microcracks (Thurner et al., 2006). However, availability of such imaging systems is limited.

The ability to detect microdamage using radiological imaging would provide a powerful set of tools to improve our understanding of the role of microdamage in bone fragility. Although microcracks are too small to be visualized using commercial micro-CT systems, contrast agents may allow a three-dimensional assessment of microdamage density and spatial distribution. The goal of this study was to validate a technique for detecting the presence of microdamage in trabecular bone using micro-CT imaging. Specifically, the aims were to: (1) develop a protocol for labeling microdamage in trabecular bone with barium sulfate ($BaSO_4$); (2) apply the technique to detect microdamage induced in bovine tibial trabecular bone specimens, and (3) correlate the micro-CT imaging results with histological measurements of microdamage.

2. Methods

Thirty cylindrical trabecular bone specimens were prepared from eight bovine tibiae. The specimens were cored along the anatomical axis of the tibia using a diamond coring drill (Starlite Industries, Bryn Mawr, PA) (Wang et al., 2004). The diameter of the specimens was 8.21 ± 0.04 mm (mean ± std. dev.). The prepared specimens were wrapped in gauze saturated with buffered saline solution and stored at −20 °C in airtight containers except during mechanical testing and labeling. Specimens were assigned to one of two groups. In group I, ten specimens were damaged by a compressive overload and subsequently treated by $BaSO_4$ precipitation. Group II (11 specimens) was not loaded, but was treated by $BaSO_4$ precipitation, and group III (nine specimens) was neither loaded nor treated.

The specimens in group I were first glued into brass endcaps (Keaveny et al., 1997), which were subsequently clamped into a servo-hydraulic load frame (model 8821s, Instron Corp. Canton, MA) for testing. Strains were measured by an extensometer (model 3550, Epsilon Technology Corp., Jackson, WY) attached to the endcaps. The effective gage length was taken as the exposed plus half the embedded length of the specimen (Keaveny et al., 1997). All tests were performed at room temperature, and the exposed portion of the specimen was wrapped in gauze saturated with buffered saline solution for hydration.

The undamaged Young's modulus of each specimen was first measured non-destructively. The specimens were loaded in compression three times from 0% to 0.4% strain at a rate of 0.5% per second, and the apparent Young's modulus was calculated from a second order polynomial fit to the stress strain data over a strain range from 0–0.2% (Morgan et al., 2001). Next, damage was induced by overloading the specimens in compression to 3% strain at 0.5% strain per second, which has been shown to induce microdamage in trabecular bone (Arthur Moore and Gibson, 2002; Keaveny et al., 1994; Wang and Niebur, 2006). The damaged Young's modulus was subsequently measured with three additional non-destructive loading cycles. Afterward, the specimens were sectioned from endcaps using a low speed diamond saw (Isomet, Buehler Ltd., Lake Bluff, IL).

The specimens in groups I and II were treated by precipitation of $BaSO_4$. Marrow was removed using a water jet while specimens were submerged in water to avoid additional damage. They were then treated by soaking in an aqueous solution of 0.5 M $BaCl_2$ (Certified ACS crystal, Fisher Scientific, Fair Lawn, NJ) for 48 h under vacuum, followed by 48 h in an aqueous solution of 0.5 M $NaSO_4$ (Anhydrous powder, Fisher Scientific, Fair Lawn, NJ) under vacuum. Finally, the specimens were agitated in buffered saline solution to remove excess $BaSO_4$ precipitates for 1 h.

All specimens were imaged by micro-CT (μCT-80, Scanco Medical AG, Bassersdorf, Switzerland) at 10 μm in-plane resolution and 10 μm slice thickness. The X-ray source voltage was 45 kVp, the source current was 177 μA, and the integration time was 400 ms per projection. Image slices were taken along the axis of the specimen, in order to capture any localized regions of damage along the length (Arthur Moore and Gibson, 2002). Ten images were captured at the specimen axis, as well as at 1 and 2.5 mm above and below the specimen axis (Fig. 1). In total, approximately 8% of the specimen volume was imaged. This protocol provided image data for a representative volume of each specimen while limiting scanning time. A $5 \times 5\,mm^2$ region (500×500 pixels) from each scan was selected for analysis to avoid the edges of the specimen, where damage might be induced during sectioning or specimen preparation. One specimen in group I was eliminated, because the sectioned length of the sample was less than 5 mm. The raw images were filtered by a Gaussian filter with $\sigma = 1$ and support 2 (Scanco, 1999).

Intensity histograms were obtained from the selected regions of each reconstructed micro-CT. The intensity histograms were fit using a double peaked Gaussian function:

$$N(I) = a_1 e^{-(I-\mu_1)^2/2\sigma_1^2} + a_2 e^{-(I-\mu_2)^2/2\sigma_2^2}, \quad (1)$$

where I is the micro-CT intensity, N is the number of voxels with intensity I, μ_1 and μ_2 are the median intensities of each peak, σ_1 and σ_2 control the peak width, and a_1 and a_2 scale the height of the peaks. The first peak represented the marrow space, while the second represented the bone tissue. The median intensity was used as a measure of $BaSO_4$ uptake in the specimens. The volume fraction of each sample was estimated by dividing the number of voxels with values in the range $\mu_2 \pm 3.5\sigma_2$ by the total number of image voxels.

Thresholding was used to determine the fraction of damaged bone tissue in each specimen. Voxels with intensities greater than 9000 (corresponding to a linear attenuation of $2.20\,mm^{-1}$) were taken to be bone tissue, and those with intensities greater than 23,500 (corresponding to a linear attenuation of $5.74\,mm^{-1}$) were taken to be $BaSO_4$ labeled damage. These thresholds were determined by parametrically varying the values and visualizing the resulting images (Fig. 2). The lower threshold was appropriate for detecting the bone tissue in untreated specimens as well as treated specimens, while no voxels exceeded the upper threshold in untreated specimens. The $BaSO_4$ labeled damage fraction ($Dx.Ar._{CT}$) was defined as the number of labeled voxels divided by the number of bone voxels.

Thin sections were prepared for histologic quantification of microdamage of the specimens in both experimental groups. No staining (e.g. basic fuchsin) was used for the histology sections, as they may have interfered with the $BaSO_4$ labeling. The specimens were gradually

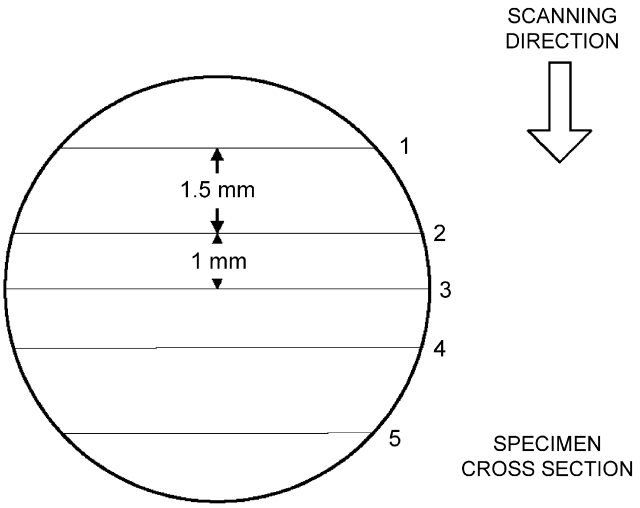

Fig. 1. At every scanning position (1–5), groups of ten images spaced 10 μm apart were obtained. One group was located at the specimen axis, two were centered 1 mm above and below the axis, and two were centered 2.5 mm above and below the axis.

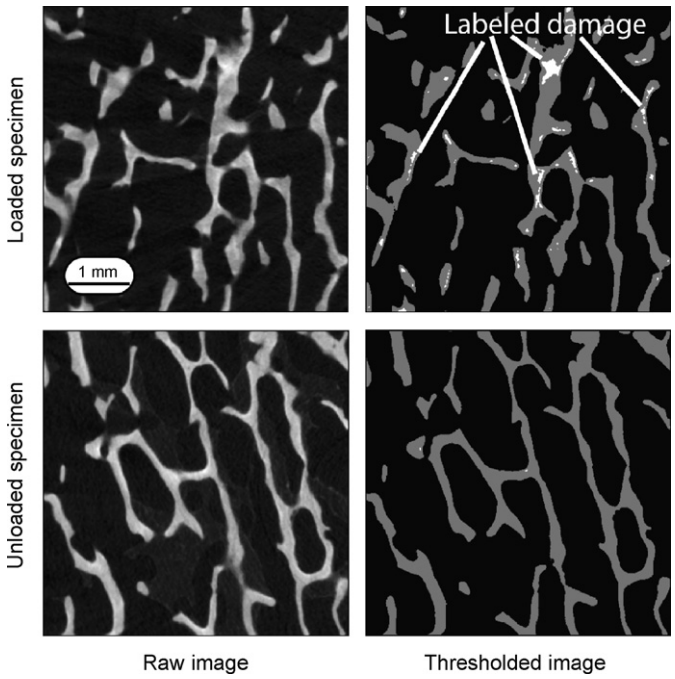

Fig. 2. Filtered (left) and thresholded micro-CT images from a loaded and an unloaded sample that were labeled with $BaSO_4$. White regions in the thresholded images represent regions with higher attenuation labeled by $BaSO_4$.

dehydrated in a series of ethanol solutions (Lee et al., 1998; O'Brien et al., 2000), then embedded in transparent polymethyl methacrylate (Aldrich Chemical Company, Inc., Milwaukee, WI) under vacuum. One 200 μm thick section was cut along the axis of each specimen using a diamond wafer saw. The surfaces of the sections were polished with a series of abrasives beginning with 600 grit paper and ending with 1/4 μm diamond paste (Phoenix Beta, Buehler, Lake Bluff, IL). The final thickness of the polished sections was approximately 150 μm. Polished sections were mounted on glass slides using Eukitt's mounting medium (American Histology Reagent Company, Inc., Hawthorne, NY) and glass cover slips. One sample from group I was eliminated because the histologic section was destroyed during processing.

The slices were imaged with reflected light microscopy (Eclipse ME 600, Nikon Inc., Melville, NY). Images of 20 randomly selected regions were captured from each section at 200 × magnification. Each image had an area of 0.39 mm^2. Microdamage was quantified in each section by area counting. A 25 × 20 grid with 28 μm edge squares was superimposed on each image (Fig. 3). The number of squares containing microcracks was counted in each section. The ratio of the number of squares containing microcracks to those containing bone was defined as the damaged area fraction ($Dx.Ar._H$). Because the histological measurement of damaged area fraction may be sensitive to the selected grid size, the analysis was repeated using a grid with 56 μm spacing.

In order to verify that $BaSO_4$ was present in damaged regions, two specimens from each treated group were imaged by back-scattered scanning electron microscopy (SEM) (Evo 50, LEO Electron Microscopy Ltd., Cambridge, UK). Back-scattered SEM provides image contrast due to compositional differences in atomic number, with increasing atomic number resulting in increased brightness. To further ensure that the increased brightness was due to the presence of barium, elemental composition was measured by electron probe microanalysis (EPMA) using energy dispersive spectroscopy (EDS) (INCA x-sight model 7636, Oxford Instruments America, Concord, MA). The relative intensity of Ba to Ca was compared between regions of high and low image brightness to verify that brightness differences were due to the presence of $BaSO_4$.

The damaged area fractions, $Dx.Ar._{CT}$ and $Dx.Ar._H$ were compared between the loaded and unloaded groups by Wilcoxon's signed rank test, because the distributions were not normal. The median intensity of the bone voxels was compared between the three groups by ANOVA with Tukey's HSD post-hoc test. Linear regression was used to relate the bone peak median intensity and $Dx.Ar._{CT}$ to $Dx.Ar._H$. All statistical analyses were performed with JMP IN version 5.1 (SAS Institute Inc., Cary, NC). The significance level for all tests was chosen as 0.05.

3. Results

Following processing, eight samples from group I, eleven from group II, and nine from group III remained for statistical analysis (Table 1).

All of the mechanically loaded specimens exhibited modulus reductions consistent with mechanical damage. The modulus decreased 12.17 ± 7.54% (mean ± std. dev.) after the compressive overload, indicating apparent level damage was induced. The initial Young's modulus was 1089 ± 464 MPa vs. 952 ± 427 MPa following mechanical loading ($p < 0.001$, paired T-test).

Microcracks were visible in the tissue matrix under both light microscopy and SEM. The mean histologically measured damaged area fraction was more than twice as high in the damaged group as in the undamaged group ($p = 0.003$, Fig. 4), verifying that damage resulted from the mechanical loading.

The micro-CT measurements of damage also indicated greater damage in the loaded group than the unloaded group. The median intensity of the bone tissue in the CT scans was approximately 6% higher in the loaded specimens than the unloaded specimens, indicating a higher uptake of $BaSO_4$ in the loaded samples ($p = 0.01$, Fig. 4). Consistent with this finding, the micro-CT measured damaged area fraction was more than 3.5 times higher in the damaged group than the undamaged group ($p = 0.015$). Both the

micro-CT measured damage fraction ($p = 0.02$, $R^2 = 0.389$) and the median intensity ($p = 0.04$, $R^2 = 0.217$) were linearly correlated with the histologically measured damage (Fig. 5).

Changing the grid size for the histological crack counting increased the predicted damage area fraction. Hence, measurement of damage was sensitive to grid size. However, differences between the loaded and unloaded groups were significant for both grid sizes. The correlation coefficients between $Dx.Ar._H$ vs. $Dx.Ar._{CT}$ and the median intensity also decreased slightly to 0.379 and 0.210, respectively.

Several microcracks surrounded by regions of increased image brightness were evident in SEM (Fig. 6). EPMA verified that the difference in brightness was due to higher relative levels of barium in the bright regions, with an intensity ratio of Ba to Ca over four times higher at the locations near microcracks compared to adjacent undamaged regions. Microcracks that were not labeled by barium were also observed, which were assumed to be artifacts caused by drying and embedding.

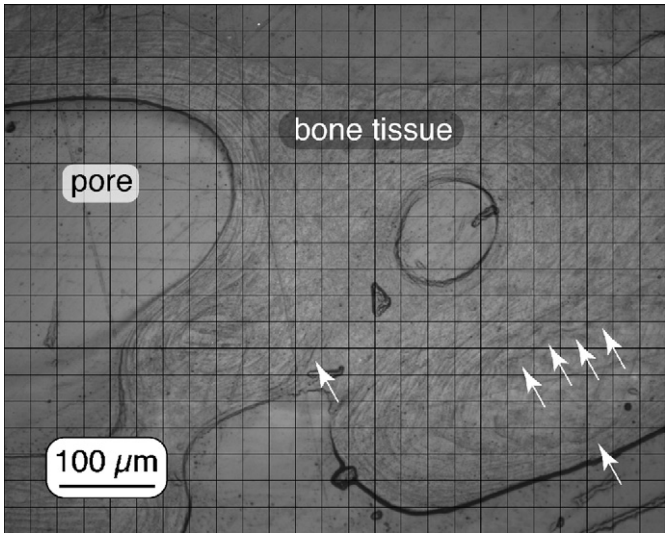

Fig. 3. A micrograph showing damaged areas (arrows). The damaged area fraction was calculated as the ratio of squares that contained microcracks to the total number of squares containing bone.

4. Discussion

A non-destructive technique for detection of microdamage in whole trabecular bone samples using micro-CT was developed. This technique, although lacking the precision of direct crack counting and measurement by histology, could allow an improved understanding of the three-dimensional relationship between damage and morphology. The positive linear regression between the median intensity and crack area and the correlation between the volume of high-intensity regions in the image and the measured damaged area fraction indicated that damaged regions were labeled by preferential precipitation of $BaSO_4$, possibly due to increased porosity that provided surfaces for nucleation and formation of $BaSO_4$ particles. The new technique cannot quantify the traditional measures of microdamage such as crack density (Cr.Dn.), crack length (Cr.Ln.), or crack surface density (Cr.S.Dn.). However, it was capable of differentiating between undamaged and damage specimens, and provided a measure that was correlated to histologically measured damage. When applied to complete three-dimensional images, this non-destructive technique has the potential to identify damaged trabeculae based on the CT intensity in order to study the morphology and orientation of damaged vs. undamaged trabeculae under different loading scenarios.

Typical microcracks have an opening on the order of 1 μm, which is an order of magnitude lower than the

Table 1
Summary of measured parameters

	Group		
	I	II	III
Description	Loaded and treated	Unloaded and treated	Control
N	8	10	9
Initial modulus (MPa)	1091 ± 410		
Damaged modulus (MPa)	965.6 ± 381		
Volume fraction (dimensionless)	0.225 ± 0.052	0.232 ± 0.056	0.205 ± 0.049
$Dx.Ar._H$ (%) small grid	1.06 ± 0.34[a]	0.49 ± 0.34[a]	
$Dx.Ar._H$ (%) large grid	2.13 ± 0.51[a]	1.04 ± 0.65[a]	
$Dx.Ar._{CT}$ (%)	4.54 ± 2.94[a]	1.23 ± 0.81[a]	0
Median CT intensity (dimensionless)	18816 ± 1089[b]	17721 ± 593[b]	14336 ± 598[b]

Values are given as mean ± std. dev.
$Dx.Ar._H$: Damaged area fraction quantified by area counting.
$Dx.Ar._{CT}$: Damaged area fraction quantified by micro-CT imaging.
[a] $p < 0.005$, Wilcoxon signed rank test.
[b] $p < 0.001$, ANOVA with Tukey's HSD test.

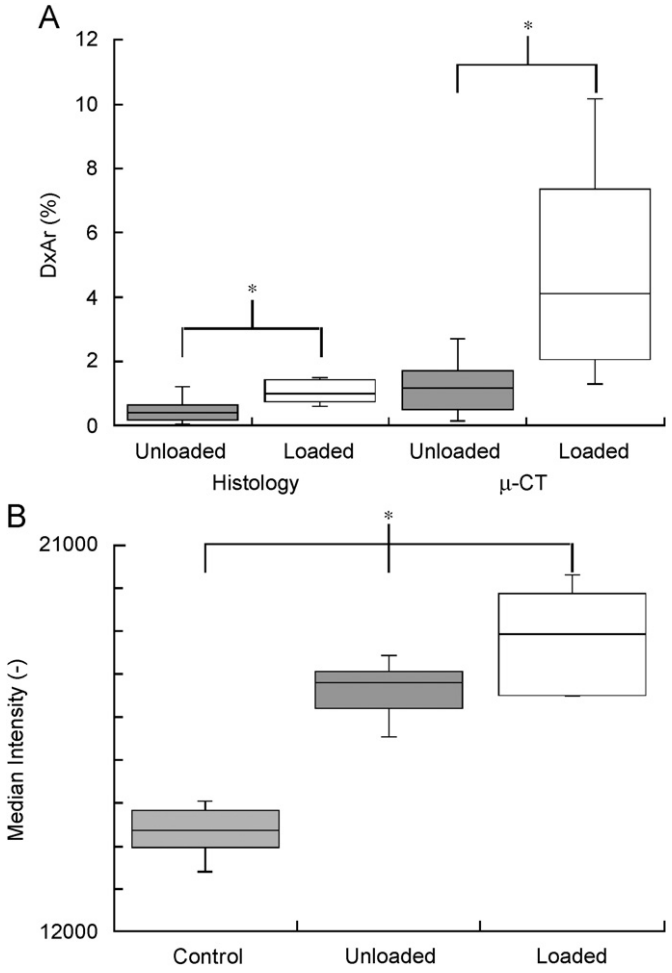

Fig. 4. (A) The mean damaged areas measured by both histology and by micro-CT were lower for the undamaged samples than for the damaged samples; (B) the $BaSO_4$ treated samples had higher median intensities than unlabeled control samples, and the loaded samples had a higher median intensity than the unloaded samples. (*Indicates significant differences across groups $p<0.02$.) The boxes in the plots bound the 25th and 75th percentiles of the data, while the bar indicates the range.

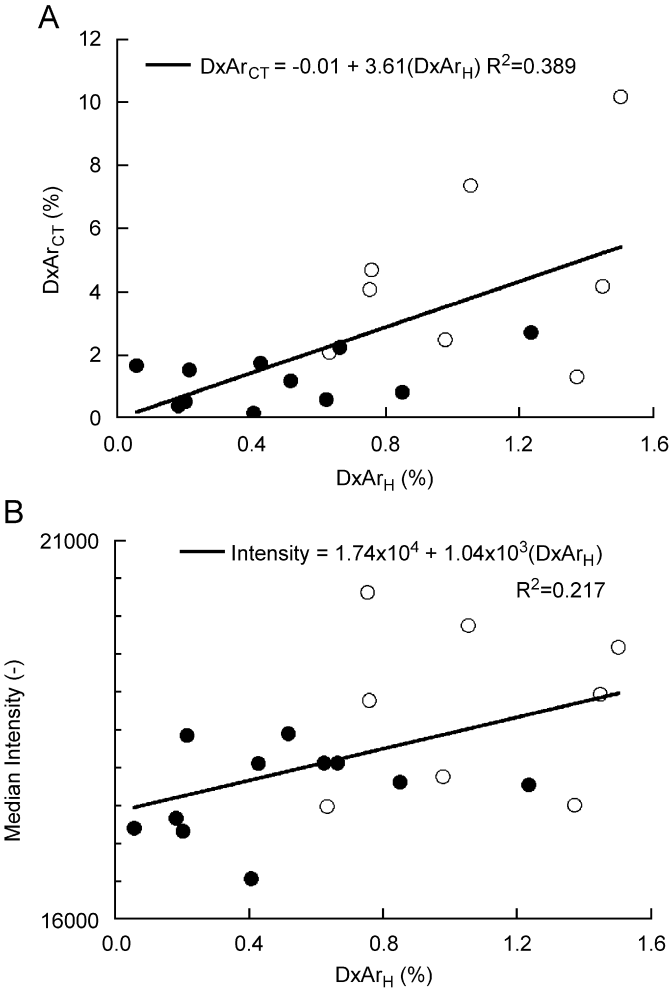

Fig. 5. The CT measured damage area fraction, $Dx.Ar._{CT}$, ($p<0.005$, A) and the median image intensity of the bone tissue ($p<0.04$, B) were both correlated with the histologically measured damaged area fraction ($Dx.Ar._H$). The open circles represent the specimens that were mechanically loaded, and the filled circles are specimens that were not loaded.

scanner resolution. However, the high X-ray attenuation of barium compared to bone, and the penetration of $BaSO_4$ into the tissue surrounding the damage, which was evident in SEM (Fig. 6), allowed the damage to be detected. These effects will result in an over estimation of the total damaged area, but can differentiate between bones with differing damage content.

The study has some notable strengths. Foremost, multiple measures were used to verify both macroscopic and microscopic damage presence in the samples. Second, linear regression was used to directly correlate the measures of damage from micro-CT with a histological technique. A parameter study was performed to ensure that the results were not an artifact of the grid size chosen for the histological measurements. From an experimental standpoint, the use of endcaps during testing reduced end effects (Keaveny et al., 1997). This testing protocol produces uniform damage patterns within the specimen cross section (Wang and Niebur, 2006; Wang et al., 2005).

There are some limitations to this study. The primary advantage of this technique is expected to be the analysis of three-dimensional damage patterns, but that was not exploited in this initial study. Instead, the initial focus was to verify the capability of the method to detect damage. However, as a result, the capability to identify the morphology of damaged trabeculae or otherwise relate damage to microstructure could not be confirmed. Second, the histological measurements would have been improved, had a stain such as basic fuchsin or alizarin been applied to the samples before dehydration and imaging. However, the $BaSO_4$ treatment may have interfered with the staining, as fuchsin also relies on precipitation within void spaces, and alizarin or other such chelating agents may also chelate to barium. Finally, the alignment of the specimens with respect to the trabecular architecture was not controlled (Wang et al., 2004). Any such misalignment would have had a minor effect in this study, but would be important to understand relationships between damage, loading mode, and trabecular architecture.

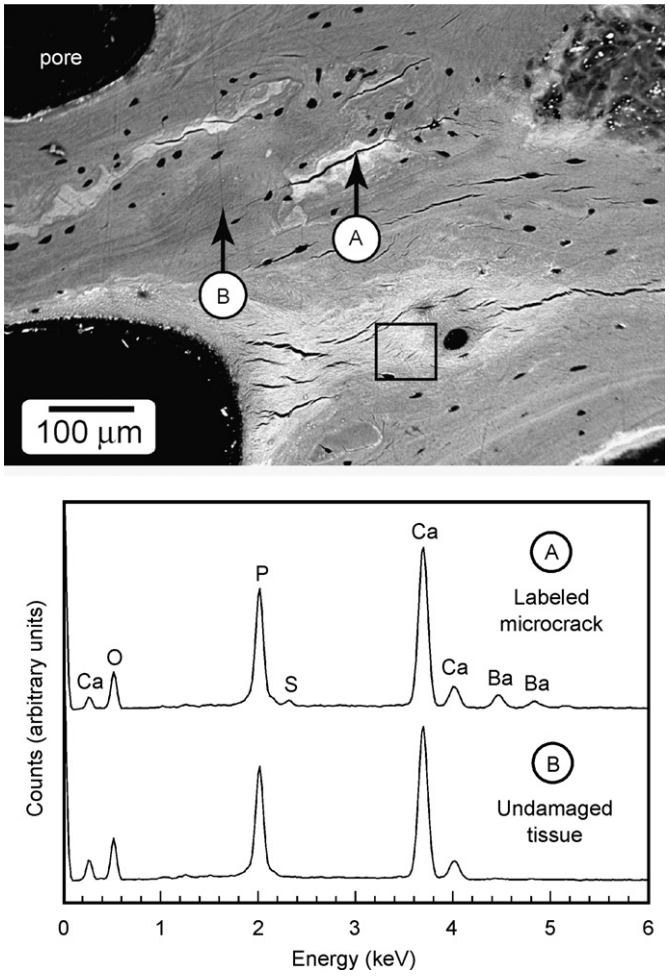

Fig. 6. A backscattered SEM image of a loaded and treated specimen showed several microcracks surrounded by bright regions. The square surrounds a region with several adjacent cracks less than 5 μm in length, which would appear histologically as diffuse damage. EDS was used to measure the elemental composition, which verified that the bright region labeled A contained a higher level of barium than the region labeled B. Cracks that are not labeled with $BaSO_4$ were considered to be artifacts caused by drying and embedding the sample for SEM imaging.

Lead sulfide (PbS) has previously been used as a contrast agent to enhance detection of microdamage in bone by back-scattered SEM (Schaffler et al., 1994). Based on the same principle employed here, individual microcracks and diffuse damage were labeled by precipitation of PbS into void spaces in the bone. The labeled regions were detected by their increased brightness in SEM, and could be visually differentiated as microcracks, diffuse damage, or anatomic features such as Haversian canals and lacunae. The limited resolution and the large volumetric data sets make it impossible to distinguish damage morphology in this way in micro-CT. However, the advantages of the micro-CT technique are the potential to image large regions and assess the three-dimensional distribution of damage with respect to the trabecular architecture and a less hazardous chemical composition.

The area counting protocol used to measure damage only gave a relative measure of the ''damaged area'' in a section. Such point and area counting techniques are common for the assessment of damage in bone, because they provide a tractable method for comparing damage levels in bones of differing loading or health histories (Fazzalari et al., 2002). To ensure that the choice of grid size did not obscure or artificially create differences in the data that did not exist, two different grid sizes were applied to the damage measurements. This analysis was not intended to verify that the area counting technique gave a true value of the damaged area, but rather to show that the correlations between the histological measurement and the micro-CT measurements were not artifacts of the grid size. The loaded samples had a larger damaged area fraction than the unloaded samples for both grid sizes, indicating that relative differences in damage levels were captured in both cases. The strength and significance of the regressions were similarly unaffected, although the coefficients were different. Hence, although both grids only approximated the true damaged area, the agreement between the two grid sizes demonstrates that the results were not an artifact of grid size.

The presence of microdamage in the unloaded specimens was probably an artifact of drying and embedding. In previous studies almost no microdamage was found in bovine trabecular bone specimens that were not subjected to mechanical loading (Arthur Moore and Gibson, 2002; Wachtel and Keaveny, 1997; Wang and Niebur, 2006; Wang et al., 2005). It is possible that the cracks in the undamaged specimens developed during specimen preparation, $BaSO_4$ precipitation, dehydration, or embedding. When using basic fuchsin staining to label microdamage, visible microcracks that are not labeled are assumed to be artifactual (Burr and Stafford, 1990). As such, the presence of cracks that did not contain $BaSO_4$ in the SEM image (Fig. 6) suggests that at least some cracks were indeed the result of drying and embedding. This artifactual damage would not be detected in the micro-CT image due to the absence of barium.

The increase in the median intensity in the undamaged specimens relative to the controls was not believed to be due to pre-existing damage in the samples, but rather to precipitation of $BaSO_4$ in lacunae and canaliculae and leaching of barium into the tissue matrix. In practice, a small control group would allow the increased intensity to be quantified so that an appropriate threshold could be selected.

The inclusion of diffuse damage in the micro-CT damaged area fraction but not in the histological measurements could have negatively impacted the correlation between the two methods. Loading to 3% apparent compressive strain is known to form both microcracks and diffuse microdamage in trabecular bone (Arthur Moore and Gibson, 2002; Wang and Niebur, 2006; Wang et al., 2005). Diffuse damage labeled by $BaSO_4$ was evident around groups of small cracks when viewed under back-scattered SEM (Fig. 6), and the thresholded images also showed focal uptake of $BaSO_4$. However, because no

labeling agents were used for the histology, diffuse damage was not detectable in the thin sections and hence could not be considered in the correlations.

The resolution of commercial micro-CT scanning systems does not allow this method to precisely image microcracks. As such, the technique is currently most powerful as a complement to microscopic techniques. However, synchrotron CT imaging can be performed at a resolution of 1 μm or less (Kinney et al., 2000; Thurner et al., 2006), and recently desktop scanners with sub-micron resolution have become available. While these systems will allow detailed visualization of individual microcracks, detecting damaged regions could be enhanced by the use of appropriate contrast agents.

Conflict of interest

None of the authors have financial or personal interests with organizations that may benefit from this work.

Acknowledgment

This research was supported by the National Institutes of Health awards AR049598 and AR052008.

References

Arthur Moore, T.L., Gibson, L.J., 2002. Microdamage accumulation in bovine trabecular bone in uniaxial compression. Journal of Biomechanical Engineering 124, 63–71.

Burr, D.B., Stafford, T., 1990. Validity of the bulk-staining technique to separate artifactual from in vivo bone microdamage. Clinical Orthopaedics, 305–308.

Burr, D.B., Martin, R.B., Schaffler, M.B., Radin, E.L., 1985. Bone remodeling in response to in vivo fatigue microdamage. Journal of Biomechanics 18, 189–200.

Fazzalari, N.L., Forwood, M.R., Manthey, B.A., Smith, K., Kolesik, P., 1998. Three-dimensional confocal images of microdamage in cancellous bone. Bone 23, 373–378.

Fazzalari, N.L., Kuliwaba, J.S., Forwood, M.R., 2002. Cancellous bone microdamage in the proximal femur: influence of age and osteoarthritis on damage morphology and regional distribution. Bone 31, 697–702.

Frost, H.M., 1960. Presence of microscopic cracks in vivo in bone. Bull Henry Ford Hospital 8, 27–35.

Keaveny, T.M., Wachtel, E.F., Guo, X.E., Hayes, W.C., 1994. Mechanical behavior of damaged trabecular bone. Journal of Biomechanics 27, 1309–1318.

Keaveny, T.M., Pinilla, T.P., Crawford, R.P., Kopperdahl, D.L., Lou, A., 1997. Systematic and random errors in compression testing of trabecular bone. Journal of Orthopaedic Research 15, 101–110.

Kinney, J.H., Haupt, D.L., Balooch, M., Ladd, A.J., Ryaby, J.T., Lane, N.E., 2000. Three-dimensional morphometry of the l6 vertebra in the ovariectomized rat model of osteoporosis: biomechanical implications. Journal of Bone and Mineral Research 15, 1981–1991.

Lee, T.C., Myers, E.R., Hayes, W.C., 1998. Fluorescence-aided detection of microdamage in compact bone. Journal of . Anatomy 193 (Pt 2), 179–184.

Lee, T.C., Mohsin, S., Taylor, D., Parkesh, R., Gunnlaugsson, T., O'Brien, F.J., Giehl, M., Gowin, W., 2003. Detecting microdamage in bone. Journal of Anatomy 203, 161–172.

Morgan, E.F., Yeh, O.C., Chang, W.C., Keaveny, T.M., 2001. Nonlinear behavior of trabecular bone at small strains. Journal of Biomechanical Engineering 123, 1–9.

O'Brien, F.J., Taylor, D., Dickson, G.R., Lee, T.C., 2000. Visualisation of three-dimensional microcracks in compact bone. Journal of Anatomy 197 (Pt 3), 413–420.

Parkesh, R., Gowin, W., Lee, T.C., Gunnlaugsson, T., 2006. Synthesis and evaluation of potential CT (computer tomography) contrast agents for bone structure and microdamage analysis. Organic and Biomolecular Chemisrtry 4, 3611–3617.

Scanco, 1999. Scanco Micro-CT Users Manual. Bassersdorf, Switzerland.

Schaffler, M.B., Pitchford, W.C., Choi, K., Riddle, J.M., 1994. Examination of compact bone microdamage using back-scattered electron microscopy. Bone 15, 483–488.

Thurner, P.J., Wyss, P., Voide, R., Stauber, M., Stampanoni, M., Sennhauser, U., Muller, R., 2006. Time-lapsed investigation of three-dimensional failure and damage accumulation in trabecular bone using synchrotron light. Bone 39, 289–299.

Wachtel, E.F., Keaveny, T.M., 1997. Dependence of trabecular damage on mechanical strain. Journal of Orthopaedic Research 15, 781–787.

Wang, X., Niebur, G.L., 2006. Microdamage propagation in trabecular bone due to changes in loading mode. Journal of Biomechanics 39, 781–790.

Wang, X., Liu, X., Niebur, G.L., 2004. Preparation of on-axis cylindrical trabecular bone specimens using micro-CT imaging. Journal of Biomechanical Engineering 126, 122–125.

Wang, X.S., Guyette, J., Liu, X., Roeder, R.K., Niebur, G.L., 2005. Axial-shear interaction effects on microdamage in bovine tibial trabecular bone. European Journal of Morphology 42, 61–70.